Schweizerische Eidgenossenschaft
Confédération suisse
Confederazione Svizzera
Confederaziun svizra

Federal Department of the Environment, Transport, Energy and Communications DETEC

Swiss Federal Office of Energy SFOE
Energy Research and Cleantech Division

Final report dated 23 November 2022

Maximum Wind Energy Production (MaxWEP)

Maximizing Winter Production of Energy by Exploiting Terrain Potential

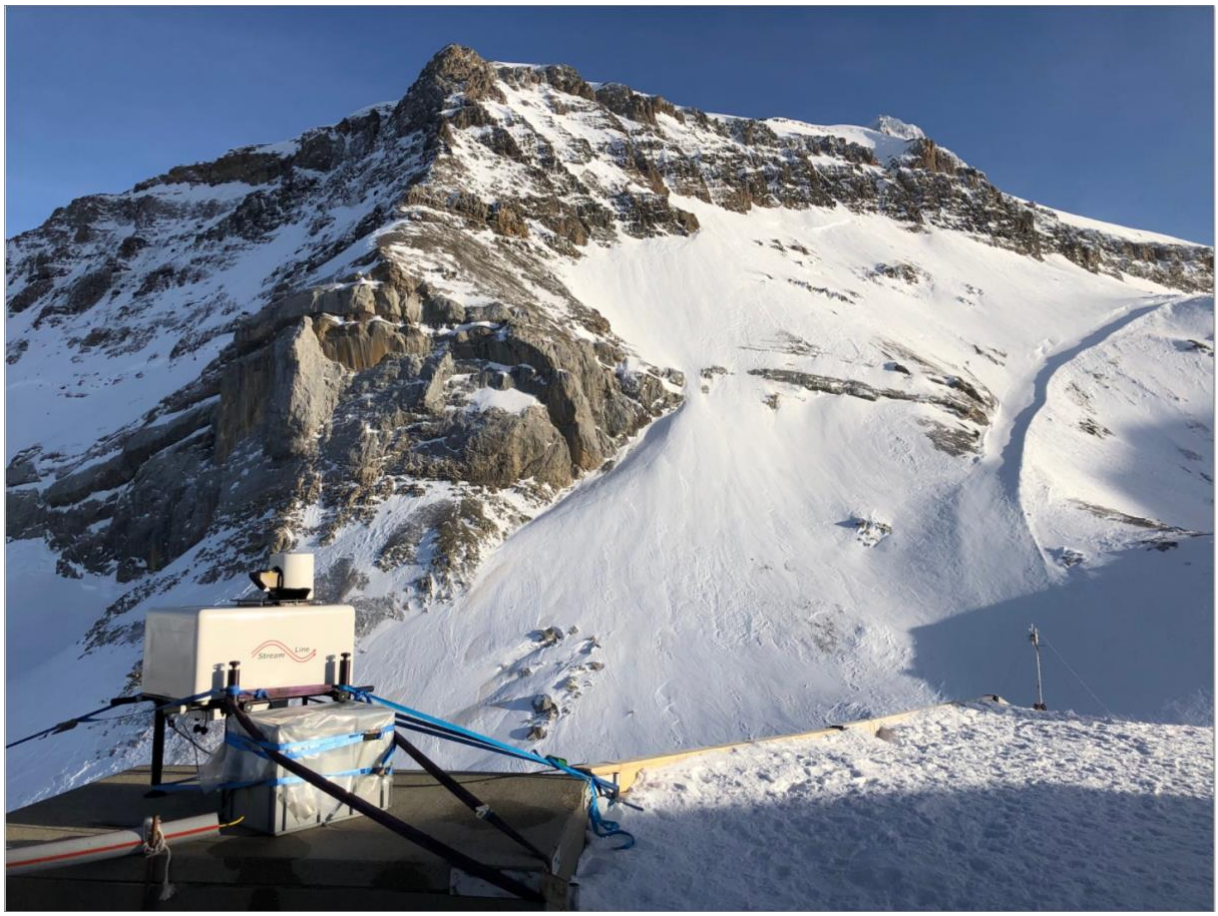

Lidar installation at Cabane, Glacier3000, Les Diablerets, VD, Switzerland. ©Huwald 2021

Date: 23 November 2022

Location: Bern

Publisher:
Swiss Federal Office of Energy SFOE
Energy Research and Cleantech
CH-3003 Bern
www.bfe.admin.ch

Subsidy recipients:
Ecole Polytechnique Fédérale de Lausanne (EPFL)
ENAC IIE CRYOS Station 2, CH-1015 Lausanne

Authors:
Fanny Kristianti, Ecole Polytechnique Fédérale de Lausanne, fanny.kristianti@epfl.ch
Franziska Gerber, WSL Institute for Snow and Avalanche Research SLF and Ecole Polytechnique Fédérale de Lausanne, franziska.gerber@slf.ch
Hendrik Huwald, WSL Institute for Snow and Avalanche Research SLF and Ecole Polytechnique Fédérale de Lausanne, hendrik.huwald@epfl.ch
Jérôme Dujardin, WSL Institute for Snow and Avalanche Research SLF and Ecole Polytechnique Fédérale de Lausanne, jerome.dujardin@epfl.ch
Sebastian W. Hoch, University of Utah, Salt Lake City, USA, sebastian.hoch@utah.edu
Michael Lehning, WSL Institute for Snow and Avalanche Research SLF and Ecole Polytechnique Fédérale de Lausanne, lehning@epfl.ch

SFOE project coordinators:
Katja Maus, katja.maus@bfe.admin.ch
Lionel Perret, lionel.perret@planair.ch

SFOE contract number: SI/501949-01

The authors bear the entire responsibility for the content of this report and for the conclusions drawn therefrom

Summary

The objective of this project has been to explore the potential of the wind over complex terrain, as an energy source during wintertime in Switzerland. A wind assessment method is developed based on short-term wind profile measurements with a wind lidar, long-duration meteorological station measurements, which are connected via machine learning to a specific site. Driving a high-resolution numerical weather model (WRF) with COSMO model as an input, we create a map of the spatial pattern of the local wind speed potential for short episodes of predominating weather patterns. We further use Wind-Topo, a very recent machine learning model, which predicts wind potential at high spatial and temporal resolution, to reproduce first the WRF simulations and then yearly averages. The yearly averages are used as a basis of comparison with the Swiss wind atlas. This report provides the local air flow analysis based on two measurement campaigns at La Stadera, near the Lukmanier Pass, GR, and at Cabane, Glacier3000 near Les Diablerets, VD, as examples of 3D wind assessment in complex terrain. Furthermore, a previous assessment in Eastern Switzerland is re-calculated with Wind-Topo. The results show that the Swiss wind atlas provides a good estimate of wind potential at the two measurement sites and that spatial patterns are comparable but not identical to Wind-Topo. The in-depth analysis of spatial patterns from both, Wind-Topo and WRF, suggest that areas of high wind potential may be missed by the wind atlas in particular in slopes and valleys. The spatial analysis presented here has limited validation and we suggest further investigation of these effects and an update of the Swiss wind atlas at higher temporal and spatial resolution. This appears necessary to assist and promote the transition of the Swiss electricity supply system towards renewable energy resources.

Contents

Abbreviations

a.s.l	Above sea level
a.g.l.	Above ground level
ASTER	Advanced Spaceborne Thermal Emission and Reflection Radiometer
COSMO	Consortium for Small-Scale Modeling
CSM	Continuous Scan Method
DEM	Digital Elevation Model
DETEC	Department of the Environment, Transport, Energy and Communications
IMIS	Inter-cantonal Measurement and Information System
LIDAR	Light Detection and Ranging
MAD	Median Absolute Deviation
MAE	Mean Absolute Error
RHI	Range Height Indicator
SNR	Signal to Noise Ratio
VAD	Velocity Azimuth Display
WRF	Weather Research and Forecasting Model

1 Introduction

1.1 Background information and current situation

After the 2011 Fukushima nuclear disaster in Japan, the Federal Department of the Environment, Transport, Energy and Communications (DETEC) has decided to re-assess the energy strategy of Switzerland into a more sustainable policy for the future. The Energy Strategy 2050 *(*SFOE, 2018*)* was developed as a response to shift towards renewable energy resources, including wind energy. Wind energy is one of the under-explored and under-exploited sources of energy in Switzerland as a majority of previous studies focuses only on flat terrain settings (Brower, 2012). The complex geographic situation of Switzerland has made it challenging to estimate the potential of wind as a source of renewable energy. Synoptic flow, the topography and the land surface type need to be considered to predict the wind characteristics (Clifton et al., 2014). Currently, the assessment of wind in complex terrain is mostly based on models of coarse horizontal resolution, which makes it challenging to include the terrain effect on 3d-atmospheric flow, i.e. wind (Grams et al., 2018; Archer and Jacobson, 2005). Switzerland's Wind Atlas (Koller and Humar, 2016) attempts to combine the WindSim model with 100 mast measurements at different locations and height. The Wind Atlas provides the annual mean wind speed at heights of 50, 75, 100, 125 and 150 m above the surface. However, it has been reported that the wind atlas has uncertainties in its results (SFOE, 2022). These uncertainties range from +/-0.5 m/s for the Jura area, +/-0.8 m/s in the central plain, +/-1.0 m/s in the pre-Alps and +/-1.5m/s in the Alps. Therefore, it is possible that there is still undiscovered potential for wind energy exploitation in the complex terrain of the Alps due to the coarse-spatial model resolution which does not sufficiently account for small-scale topographic effects.

1.2 Purpose of the project

This project aims at exploring different methods to estimate the local wind energy potential in the complex terrain of Switzerland. We try to find spatial-temporal wind patterns that would not be represented in previous assessments. We propose a combination of locally measured wind data with numerical simulation, and a sophisticated machine learning technique, to investigate the potential of the wind energy harvesting in the complex alpine terrain.

1.3 Objectives

1. Understanding the effect of complex terrain on 3D wind in the alpine region of Switzerland using a combination of Light Detection and Ranging (LIDAR) measurements, climatological analysis of IMIS weather station data, atmospheric numerical simulations and machine learning.
2. Approximation of the annual yield and characterization of the spatial and temporal variability of wind energy potential as a function of the local dominant weather patterns.

2 Description of Facility

The first campaign was conducted at La Stadera, on a north-west facing slope of Piz Scopi near the Lukmanier Pass, GR, Switzerland at 2519 m a.s.l. (705783, 160126), from 20/10/2020 to 16/12/2020. The second campaign was conducted at the Cabane cable car station of Glacier3000, VD, Les Diablerets, Switzerland at 2523 m a.s.l

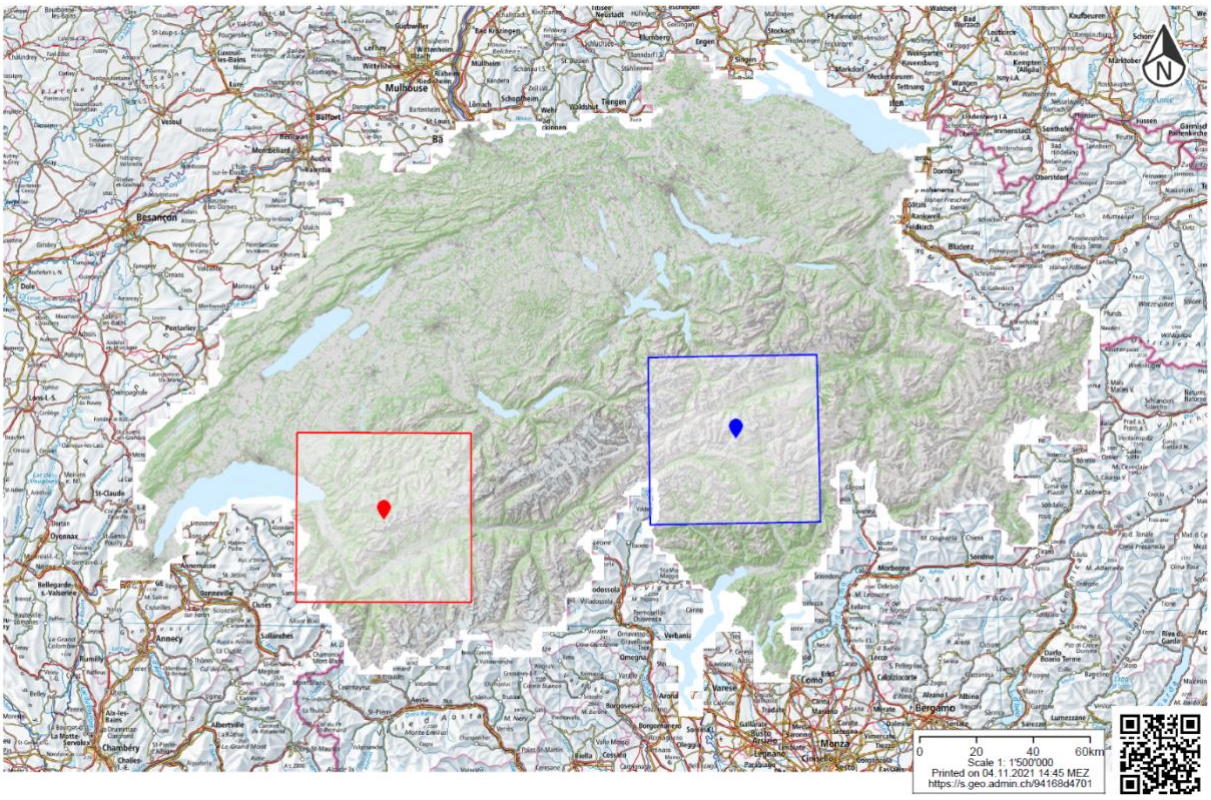

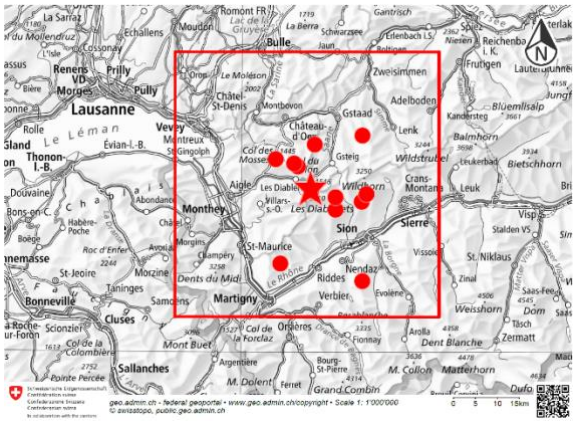

(582773, 132080), from 20/02/2021 to 02/05/2021. Both sites are located in complex alpine terrain of Switzerland. The Stadera site is located in the eastern part of Switzerland (blue marker, Figure 1a) and the Cabane site is located in the western part of Switzerland (red marker, Figure 1a). Table 1 summarizes further characteristics of the two campaign sites.

(a)

(b)

(c)

Figure 1 (a) Campaign location at Lukmanier (blue marker) and Les Diablerets (red marker). The red and blue square represent the domain size for the WRF-COSMO1 simulations for Lukmanier and Les Diablerets, respectively. Detailed maps of the campaign locations Les Diablerets including the measurement locations marked by the star symbols and the surrounding IMIS station by the dot symbols are given for Lukmanier (b) and Les Diablerets (c). Source: swisstopo.

Table 1 Details of the Lukmanier and Les Diablerets field campaigns

Sites	Lukmanier	Les Diablerets
Campaign duration	20/10/2020 – 16/12/2020	20/02/2021 – 02/05/2021
LIDAR position (WGS84 and CH1903 coordinate system)	46.58404, 8.81885 (705783, 160126)	46.33989, 7.21490 (582773, 132080)
Height above sea level	2519	2523
Max. horizontal wind speed during campaign at 100 m a.g.l. from LIDAR	31.14 m/s	29.36 m/s
Max. horizontal wind speed during campaign from Sonic	14.4 m/s	18.71 m/s
Averaged horizontal wind speed during campaign at 100 m a.g.l. from LIDAR	5 m/s	4.58 m/s
Averaged horizontal wind speed during campaign from Sonic	3.1 m/s	3.0 m/s

3 Procedures and methodology

A Halo Photonics Streamline scanning Doppler wind Lidar instrument and a Campbell Scientific CSAT3 3D ultra-sonic anemometer were deployed during the two measurement campaigns. The applied method uses the combination of a machine learning (ML) model, numerical simulations with the Weather Research and Forecasting, WRF, model (WRF, Skamarock, 2019) driven by Consortium for Small Scale Modelling simulations, COSMO1, (MeteoSwiss) simulation output, measurements from the Inter-cantonal Measurement and Information System (IMIS) stations, and data from the above-mentioned field-based measurement campaigns. Also, data from a previous third-party observational wind energy campaign at the Lukmanier Pass field site 'La Stadera' by Meteotest (Meteotest, 2016) is used for comparison and validation of our analysis. The spatial variability of wind speed is estimated by WRF-COSMO1 model simulations and the wind potential is estimated by using a machine learning model. The machine learning Wind-Topo model (Dujardin and Lehning 2022) is further used to compare the spatio-temporal wind characteristics to WRF simulations and the wind atlas.

3.1. Data Sampling Configuration

During the Stadera campaign, the CSAT3 3D ultra-sonic anemometer was installed at 2.4 m above ground with an azimuth angle of 302° and was programmed to collect samples at a frequency of 20 Hz. It is installed at approximately 4 m horizontal distance south of the LIDAR instrument. At the Cabane site, the CSAT3 was installed at 2.5 m above ground with an azimuth angle of 172° and was programmed to collect samples at a frequency of 10 Hz. The anemometer was located at approximately 20 m horizontal distance south of the LIDAR instrument. Further instrument setup details for both sites can be seen in Figure 2a and 2b.

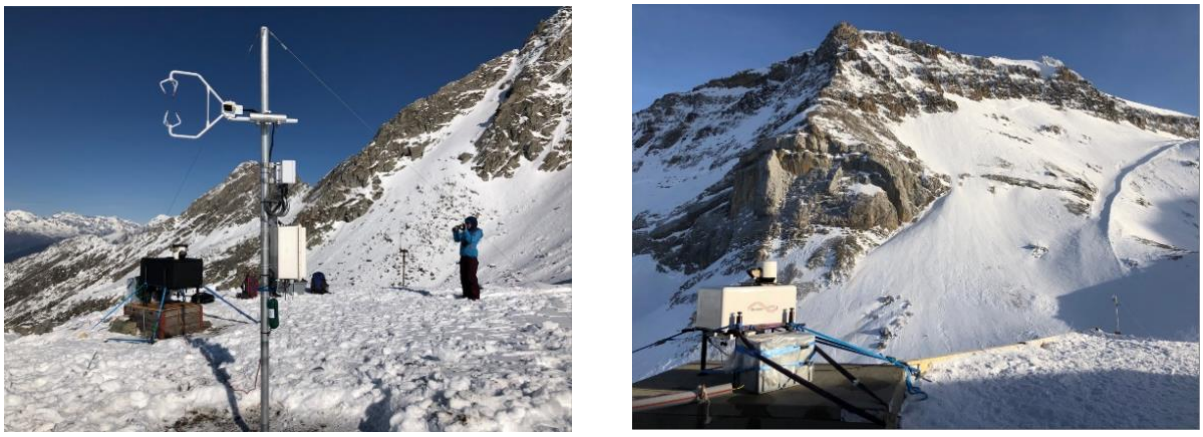

(a) (b)

Figure 2 Instrument setup (a) at the Stadera site and (b) at the Cabane site. (a) shows the sonic anemometer in the foreground and the LIDAR instrument (thermally insulated) in the background. (b) shows the LIDAR instrument in the foreground and the sonic anemometer on the mast in the background.

The range gate length of the LIDAR is set to 30 m with a gate number of 1400 and the gate overlapping options activated. LIDAR measures the doppler retrieval in the atmosphere in segmented parts called gates. The combination of the number and range of gates will define the measurement range, which is the maximum distance that the LIDAR is able to measure. Gate overlapping means stacking the gate center with some overlapping distance between gates. This method will enable us to gain extra distance from the blind region of the lidar. The blind region is a few closest gate ranges that is contaminated with signal noise.

For the Stadera field campaign, the scan sequence consists of (1) a vertical stare scan, (2) a wind profile Velocity Azimuth Display (VAD6) scan at 70° elevation angle, followed by four user-defined scans. These four user-defined scans are: (a) a conical scan using the Continuous Scan Method (CSM) at 27° elevation angle, (b) a conical scan at 27° and 45° elevation angle in step-stare mode at 30° azimuth intervals, (c) a conical scan at 45° and 70° elevation angle using the CSM mode, and (d) a conical scan at 70° elevation angle in step-stare mode with 30° azimuth intervals. In the conical scans, the elevation angle is fixed to a constant angle while the azimuth is varied according to the scanning method. This scan sequence was repeated at 5 minutes time intervals.

The LIDAR configuration during the Cabane field campaign uses the same gate number and gate length as the Stadera campaign. The scan sequence for the Cabane campaign consists of: (1) a vertical stare scan, (2) a wind profile VAD6 scan at 70° elevation angle and two user-defined scans. The user defined scans are (a) a Range Height Indicator (RHI) scan at 200° azimuth angle, and (b) a feedback RHI scan. The feedback scan allows the LIDAR to get an RHI scan which is aligned with the direction of the maximum wind speed according to the result of the previous wind profile VAD6 scan. Scan sequences from the Stadera and Cabane sites are presented in Table 2. Detailed terrain features at Stadera and Cabane can be seen from Figure 3 where the red star symbols indicate the instrument location.

Table 2 LIDAR configuration

LIDAR configuration	
Lukmanier Campaign Site	Les Diablerets Campaign Site
1. Vertical stare, azimuth=90° 2. VAD6, elevation angle=70° 3. Conical user defined scans a. CSM, elevation angle=27° b. step stare, elevation angle = 27° and 45° c. CSM, elevation angle 45° and 70° d. Step stare, elevation angle = 70°	1. Vertical stare, azimuth=90° 2. VAD6, elevation angle=70° 3. User defined scans a. RHI, azimuth angle=200° b. Feedback RHI scan

Table 3 LIDAR post processing filters

Blind region filter	Removal of all data within 60 m of radial distance from the LIDAR
SNR filter	Removal of data with SNR < 1.02
MAD filter	Removal of data outside the upper and lower limit of the MAD filter
Data distribution filter	Each of the specified 6 bins needs to have at least one data point inside, except VAD6 measurement method
MAD fit filter	Removal of data outside the upper and lower limit of the MAD fit limit
Number of data filter	Removal of the fit containing number of data less than the limit as specified below: a. Step stare mode limit is minimum 8 out of 12 data points. b. CSM mode limit is minimum 50% of the number of data points compared to the original number of data. c. VAD6 only considered valid if all 6 data points pass the previous filter.
R square filter	Removal of wind speed with R square coefficient less than 0.7 for the sine curve fit

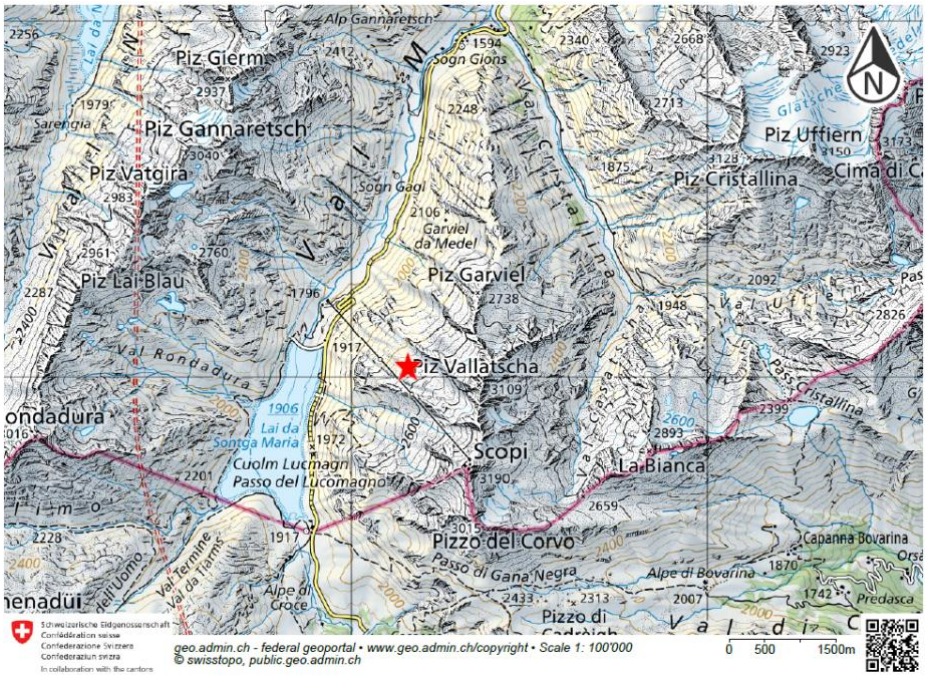

(a)

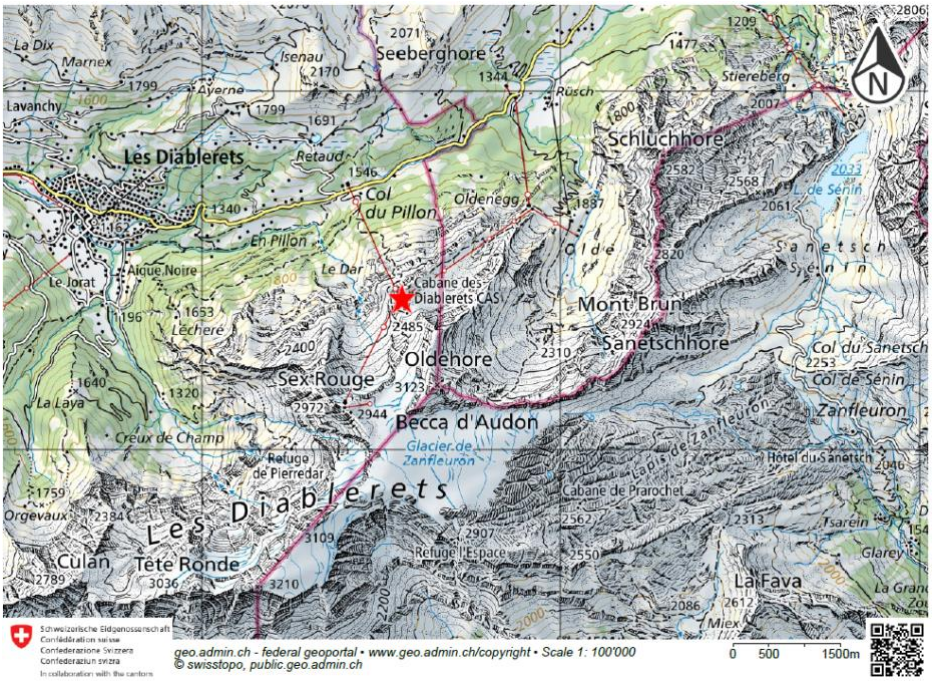

(b)

Figure 3 Detailed terrain situation from Lukmanier (a) and Les Diablerets (b) campaign. Source: swisstopo

3.2. Temporal Wind Speed Prediction

The prediction of wind speed time series is obtained using the LIDAR measurements, combined with data of surrounding operational weather stations. The combination is achieved by using a machine learning algorithm as detailed in Section 3.2.2.

3.2.1. LIDAR Post-Processing

The raw LIDAR data is filtered using several filters according to Table 3. The first filter is the blind region filter, which removes all data within the first 60 m radial distance from the LIDAR. The second filter is the signal-to-noise ratio (SNR) filter, which eliminates the data with SNR numbers less than 1.02. The SNR number is picked such as it eliminates the noise and keeps the good quality data from the measurement. The third filter is the Median Absolute Deviation (MAD) filter, which represents the absolute median of the distance from the data point x_i to the median of the Doppler velocity $\langle x \rangle$ (see Equation 1). The data point needs to be inside the MAD limits to pass the MAD filter. The MAD limits are defined by the MAD number multiplied by the coefficient q_{MAD} (Equation (2)). This coefficient is set to 7 for this study. The coefficient number is chosen to filter out the outliers of the data and keeps the data that is within acceptable range to the MAD value.

$$MAD = \langle |x_i - \langle x \rangle| \rangle \tag{1}$$

$$\langle x \rangle - MAD.q_{MAD} \leq x_i \leq \langle x \rangle + MAD.q_{MAD} \tag{2}$$

The next filter is the data distribution filter to ensure that there is a good spread of data for each bin. Based on the VAD scan, we defined 6 as the number of bins, with bin widths of 60 azimuth degrees. No empty bin is allowed in order to prevent an underrepresentation of certain azimuth directions and hence large gaps between the data points. An exception is made for the VAD6 method due to the limitation of data points, therefore an exception of allowing one empty bin is applied for the VAD6 post processing. After applying this filter, all remaining data should have a good sinusoidal distribution. A sine curve is fit to the remaining data with assumption of horizontal homogeneity of wind vector applied. To eliminate the data points with far distance to the sine fit, a modified MAD filter (MAD fit filter) is applied. The MAD fit filter includes calculating the median of distance from the data point x_i to the sine curve, instead of the median. Then we calculate the MAD from the new median value from the fit.

After applying all filters, the final fit is only applied for the gate ranges which still have a good amount of data based on the scan method. For VAD6, only 5 data points need to pass all the filters. For the step stare method, we define that the minimum number of data points needed is 8 out of 12 total step stare data points. For the CSM method, a minimum of 50% of the original number of data points is required. The final filter is the R^2 filter, where the R^2 coefficient needs to be at least 0.7 to be considered valid. The R^2 coefficient indicates the quality of the correlation of the data points and the sine fit. The larger R^2 the better the curve fit. All steps of the LIDAR data post-processing are graphically summarized in the flowchart of Figure 4.

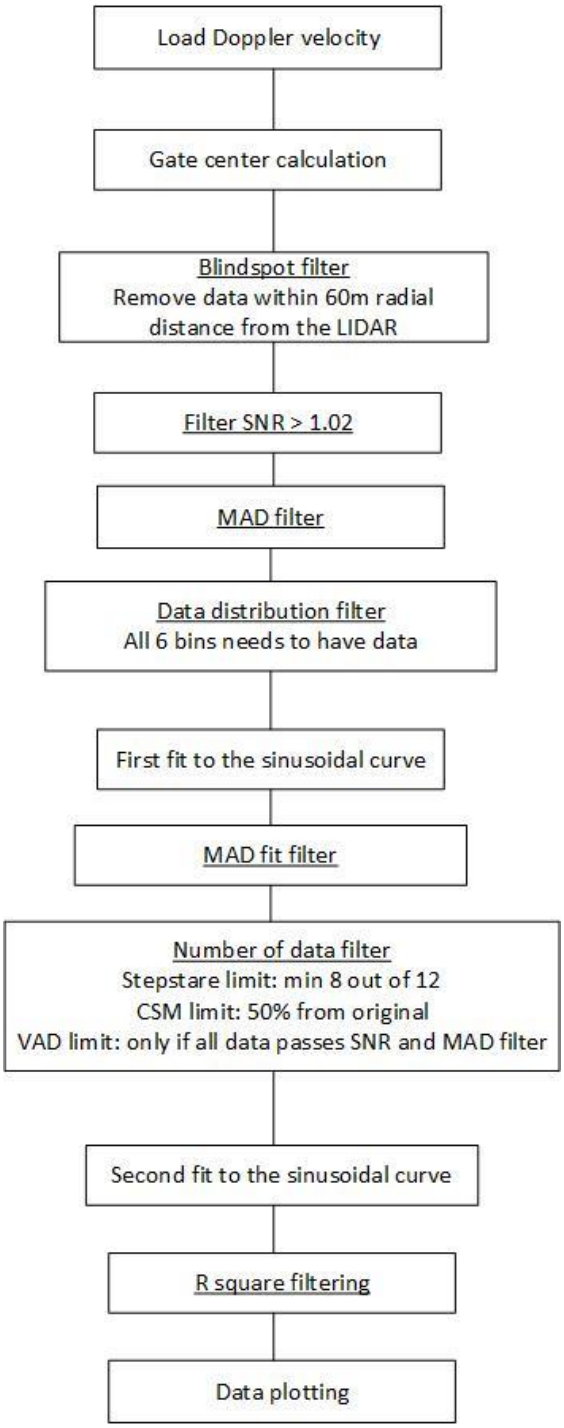

Figure 4 LIDAR data Post processing LIDAR Flowchart

3.2.2. Data Combination by Machine Learning

Wind speed assessment is obtained by applying a machine learning (ML) algorithm, more specifically a neural network, to predict a long time series of wind speed using the surrounding IMIS station data as predictor. The selection of IMIS stations is based on the proximity to the LIDAR locations. There are 13 stations selected for the Stadera site and 12 stations for the Cabane site (Tables 4 and 5). The neural network is trained to find the relationship between the vertical profile of wind speed measured by the LIDAR and the corresponding measurement from the IMIS stations. Then, this relationship can be used anytime when measurements from the corresponding IMIS stations are available to predict the wind profile at the LIDAR site. Two versions of the neural network are used. In the first one, the horizontal wind components u and v are used. The second one only uses the wind speed.

This machine learning model requires all IMIS data for a given time step to be available in order to make a prediction. Consequently, any data gap in one of the IMIS stations prevents the model to generate a prediction. A strategy to fill the IMIS data gaps is thus required if one is to generate complete time series of vertical profiles of wind speed. A dedicated data filling technique was developed. Using times during the measurement campaign when all IMIS stations provide data, optimal scaling factors are determined for each IMIS station to minimize the Mean Absolute Error (MAE, Equation 3) with the predicted wind speed (v_{ML}). When the ML model is used to generate a vertical profile for a time when some input (IMIS) data is missing, the missing values can be estimated by using a weighted average of all available data by the optimal scaling factors.

$$MAE = \frac{\sum_i^n |v_{ML} - v_{IMIS}|}{n} \quad (3)$$

Table 4 IMIS stations at Lukmanier domain

Lukmanier Area			
Station	Region	Lon (E)/Lat (N)	Elev. (m a.s.l.)
ANT	Andermatt	8°34′50”/46°37′51”	1438
COM	Acquarossa/Comprovasco	8°56′08”/46°27′34”	575
DIS	Disentis	8°51′12”/46°42′24”	1197
GOS	Göschenen	8°35′43”/46°41′34”	950
GUE	Gütsch/Andermatt	8°36′54”/46°39′09”	2286
MTR	Matro	8°55′29”/46°25′36”	2171
PIO	Piotta	8°41′17”/46°30′53”	990
SLFDT2	Dötra/Preda	8°52′08”/46°32′35”	2060
SLFDTR	Dötra/Costra	8°51′58”/46°32′53”	2391
SLFLU2	Lukmanier/Lai Verd	8°46′59”/46°36′14”	2550
SLFLUK	Lukmanier/Piz Gannaretsch	8°47′11”/46°36′43”	3040
SLFPU2	Puzetta, Medel/Ils Plauns	8°51′45”/46°37′34”	2195
SLFPUZ	Puzzeta, Medel/La Muota	8°51′25”/46°37′22”	2425

Table 5 IMIS station at Les Diablerets area

Cabane Area			
Station	Region	Lon (E)/Lat (N)	Elev. (m a.s.l.)
CDM	Col des Mosses	7°05′54”/46°23′29”	1412
DIA	Les Diablerets	7°12′14”/46°19′36”	2964
SLFCH2	Chaussy/Pierres Fendues	7°09′50”/46°22′36”	2220
SLFCHA	Chaussy/La Para	7°09′09”/46°22′58”	2540
SLFCON	Conthey/Etang de Trente Pas	7°16′31”/46°17′20”	2230
SLFDIA	Les Diablerets	7°16′30”/46°18′51”	2575
SLFFUL	Fully/Grand Chavalard	7°06′47”/46°10′43”	2898
SLFLAU	Lauenen/Lauenehore	7°21′16”/46°26′25”	2477
SLFNEN	Nendaz/Creppon Blanc	7°21′15”/46°08′35”	2714
SLFOBM	Gstaad/Ober Meiel	7°12′48”/46°25′18”	2110
SLFVD2	Arbaz, Val. Sionne/Donin du Jour	7°21′59”/46°19′15”	2390
SLFVDS	Arbaz, Val. Sionne/Crêta Besse	7°21′8”/46°18′19”	2696

3.3. Spatial Analysis for Local Wind Energy Potential with WRF

We further study the spatial patterns of the flow mechanisms for the surroundings of the measurement campaign locations, which could not be captured by our profile measurements at a single point. Representative flow situations are chosen based on the principal wind directions identified from the CSAT3 and LIDAR data. For the Stadera site, a northeasterly (09/12/2020) and a southwesterly (23/10/2020) flow case are chosen as representative examples. For the Cabane site, a southwesterly (27/02/2021) and a northeasterly (11/03/2021) case are chosen.

The WRF model (WRF, Skamarock, 2019) version 4.1.5 initialized and driven by MeteoSwiss COSMO1 simulation output (WRF-COSMO1, hereafter) is used to investigate spatially distributed potential for wind energy production in alpine complex terrain. For the analysis at each measurement site two days were selected, representing the predominant wind direction at that site during the campaign period. The topography input is based on the Advanced Spaceborne Thermal Emission and Reflection Radiometer (ASTER) global digital elevation model (DEM) v003 (NASA/METI/AIST/Japan Space systems and U.S./Japan ASTER Science Team, 2019), and the land use is taken from the Coordination of Information on the Environment (CORINE) dataset (European Environmental Agency, 2006) as provided by Gerber and Lehning, 2021. The 1-2-1 weighted average smoothing technique is applied to reduce all slope angles below approximately 45°. For the Stadera simulation, 8 cycles of the smoothing process are performed. The Cabane simulation is conducted with 5 smoothing cycles. After this process, the maximum slope in the Stadera domain is 45.7° and the maximum slope in the Cabane domain is 44.9°.

The simulation is run with one domain with no nesting based on the recommendation by Chow et al. (2019), centered around the LIDAR location (star symbols, Figure 1b, 1c). The domain size is 60 km x 60 km with a horizontal resolution of 200 m (i.e. 301 x 301 grid point in the horizontal direction). There are 100 vertical levels up to 15’000 hPa using eta-coordinates. The simulation time step is 0.1 seconds. The planetary boundary layer physics schemes use the Shin-Hong Scale scheme (Shin and Hong, 2015). The microphysics are parameterized using the Morrison 2-moment scheme (Morrison et al., 2009) with no cumulus options applied. Long- and shortwave radiation is calculated with the ‘rrtmg’-scheme (Lacono et al., 2008). The surface layer scheme uses the Monin-Obukhov parameterization combined with the Carlson Boland viscous sub-layer (Jimenez et al., 2012),

while land surface processes are parameterized by the Noah-MP scheme (Niu et al., 2011 and Yang et al., 2011). The simulation setup is summarized in Table 6.

3.4. Spatial Analysis for Local Wind Energy Potential with Wind-Topo

We adapted the model Wind-Topo (Dujardin and Lehning, 2022) to predict not only surface wind fields but also wind fields at 100 m agl, which is more relevant for wind exploitation. The conversion of the outputs of Wind-Topo (wind speed at 10 m agl) to the desired wind speed at 100 m agl uses the statistical relationship between wind speed at those two heights in COSMO-1. Specifically, a quantile mapping function is generated for every grid cell and it links the distributions of wind speed at those two heights. Then, for each grid cell, this mapping function is applied to the 10 m agl Wind-Topo outputs. The adapted model serves to bridge between the spatial WRF simulations and the wind atlas, which only gives yearly averages. To be able to not only assess spatial patterns for specific weather situations as simulated by WRF but also extract yearly averages, Wind-Topo was run at hourly resolution for the target areas and the year 2017. This means that within the uncertainty of the year to year variability, the Wind-Topo results should be comparable to the Swiss wind atlas. We present spatial maps of Wind-Topo for the same situations as simulated with WRF (see above) and in addition for the entire year 2017. The comparison with WRF allows a (limited) validation and the comparison with the wind atlas allows to see, where there are differences in the spatial patterns of wind potential estimates.

4. Results

4.1. Near-surface Wind Measurement

In this section, we investigate the necessary information regarding the terrain effects and local wind characteristics from the 3D sonic anemometer (CSAT3). We use the CSAT3 data as representative of the near ground flow characteristics. The study of the near-surface winds is the first step to analyze the complex terrain flow. The result from the CSAT3 measurements are then compared with the data from the LIDAR instrument as well as the WRF-COSMO1 numerical simulation.

The main wind directions near the ground measured by the CSAT3 were found between the northeast and southeast for the Stadera site, and mainly west for the Cabane site, respectively (Figure 5). The time series of horizontal wind speed at both campaign sites is shown in Figure 6a,b. The average near-surface wind speed for the two sites, Stadera and Cabane, and for the deployment periods was 3.1 m/s and 3.0 m/s, respectively. At the Stadera site, a maximum near-surface wind speed of 14.4 m/s from 150° (SSE) was recorded on 05/12/2020 at 05:04am at the Stadera site. At Cabane, a maximum near-surface wind speed of 18.7 m/s from 255° (WSW) was recorded on 21/03/2021 at 00:42am.

The largest values of negative vertical wind speed are associated to winds from the sector 90–180° (Figure 6c,e). This agrees with the majority of high horizontal wind speed from the north-easterly sector (Figure 5a). This reflects the synoptic wind either from the northerly or southerly direction influenced by Piz Vallatscha / Scopi mountain and forced to flow parallel to the terrain contour lines (Figure 3a). Minor sectors of wind direction are located from northeast to southeast. Most of the vertical wind speed component at the Stadera site is negative, which shows the strong terrain effect at the measurement location (Figure 6c). For example, the winds from the NE or SE sectors may be superimposed by katabatic winds down the slopes of the Piz Vallatscha / Scopi mountain. overall resulting in a rather systematic predominant downward wind speed component during flow from these directions.

Table 6 WRF-COSMO1 simulation setup

Horizontal grid resolution (dx,dy)	200 meters
Horizontal domain	301 x 301 grid points (60 x 60 km)
Number of vertical levels	100
Time step (dt)	0.1 seconds
Top domain pressure	15'000 hPa
Microphysics scheme	Morrison 2-moment
LW and SW radiation scheme	rrtmg
Surface layer scheme	MO similarity with Carlslon Boland
Topography smoothing	1-2-1 smoothing scheme
Land-surface scheme	Noah-MP

The correlation of the vertical and horizontal wind speed (Figure 6e) appears to be divided into three main wind regimes: (a) Sector 0–90° (blue and orange dots), (b) Sector 90–180° (green and red dots), and (c) Sector 270–360° (pink and light green dots). The correlation category represents the different characteristics of wind speed according to the local topography around the CSAT3 instrument. Regime (a) shows strong horizontal components largely dominating over the vertical component. The relatively smaller vertical component is seen as a result of the principal wind which is aligned with the terrain contours of Piz Scopi mountain. A stronger vertical wind component is observed when the wind is more perpendicular to the terrain contour lines of Piz Scopi mountain.

In Regime (b) we observe a strong negative correlation between vertical and horizontal wind speed. This sector represents the deviated synoptic wind from a southerly direction as well as katabatic wind down the western slope of Piz Vallatscha / Scopi. Regime (c) shows positive vertical components with rather moderate horizontal velocity, compared to the other previously mentioned regimes. This sector represents valley winds from northwest direction which are then forced to move upslope because of the orographic obstacle.

The 3 regimes are also visible in the figures showing the correlation of vertical wind speed and wind direction (Figure 6g). The light blue color represents the wind speed during the daytime of 9h – 21h and the purple color during the nighttime of 21h – 9h. When separating the wind speed based on the diurnal cycle, a slight increase of the downward vertical wind speed amplitude during the daytime can be seen. This shows the diurnal effect at the Stadera site, especially for the sector 100–200° for the downward vertical wind direction.

At the Cabane site, the 3D sonic anemometer was also installed. At that site, winds are mostly blowing from the west, with a secondary wind direction from the northeast to southeast (Figure 5b) being typical for cold and dry flow (bise) and warm and dry flow (Föhn), respectively. The westerly wind is the dominant synoptic wind intercepted and affected by the Diablerets mountain (Figure 3b). When the synoptic wind reaches the Diablerets mountain, it experiences a strong orographic lifting. The maximum wind speed of 14.4 m/s during the two months observation period was measured during a west wind event, i.e., for the main wind direction. Figure 6b,d, illustrates the large positive vertical velocity from the west linked to high horizontal flow velocity.

The correlation between vertical and horizontal wind speed is shown in Figure 6f. The positive vertical wind speed increases with increasing wind speed in the wind direction sector 270–360° (pink and light green dots). The other sectors show moderate vertical wind speed components: N to NE slightly positive (blue dots), NE to SE slightly negative but with strong horizontal wind speeds (orange and green dots) and SE to S slightly negative with weaker horizontal wind speeds (red dots). Positive vertical wind speed components are observed mostly for winds from

the sector 225–360° (SW to N), which is coherent with the impact of the orographic obstacle. Winds with a negative vertical component are observed for directions 45–225°, which is coherent with the sloping terrain. The southerly wind may have two different origins: (a) strong Foehn winds crossing the Diablerets mountain massif and (b) cold katabatic winds draining the Zanfeuron glacier.

4.2. Characteristics of Local Wind Flow Above Ground

The local wind characteristics at the range of heights, where wind turbines are typically operated (order of 100m above ground) is studied further in this section. The local near-surface wind characteristics from Section 4.1 are compared with results the LIDAR measurements collecting data at higher levels above ground. This comparison will serve as a synthesis of the local near-surface wind characteristics at the campaign sites as well as aloft at the typical range of wind turbine hub heights

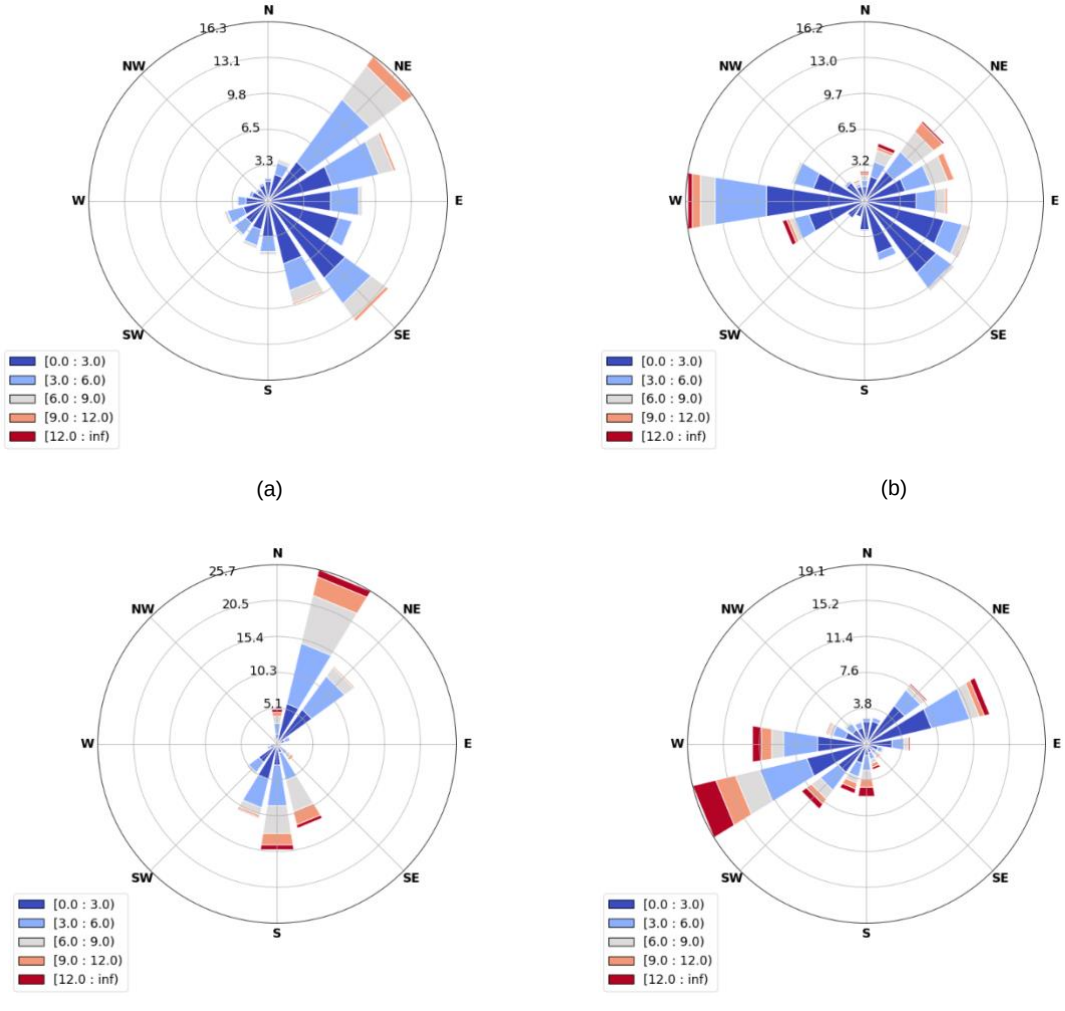

Figure 3 Wind roses based on 3D ultra-sonic anemometer measurements (a) between 20/10/2020 and 16/12/2020 at the Lukmanier site and (b) between 20/02/2021 and 02/05/2021 at Les Diableretsthe Les Diablerets site. Wind roses based on LIDAR measurement at 100 m a.g.l. (c) between 20/10/2020 and 16/12/2020 at the Lukmanier site and (d) between 20/02/2021 and 02/05/2021 at the Les Diablerets site

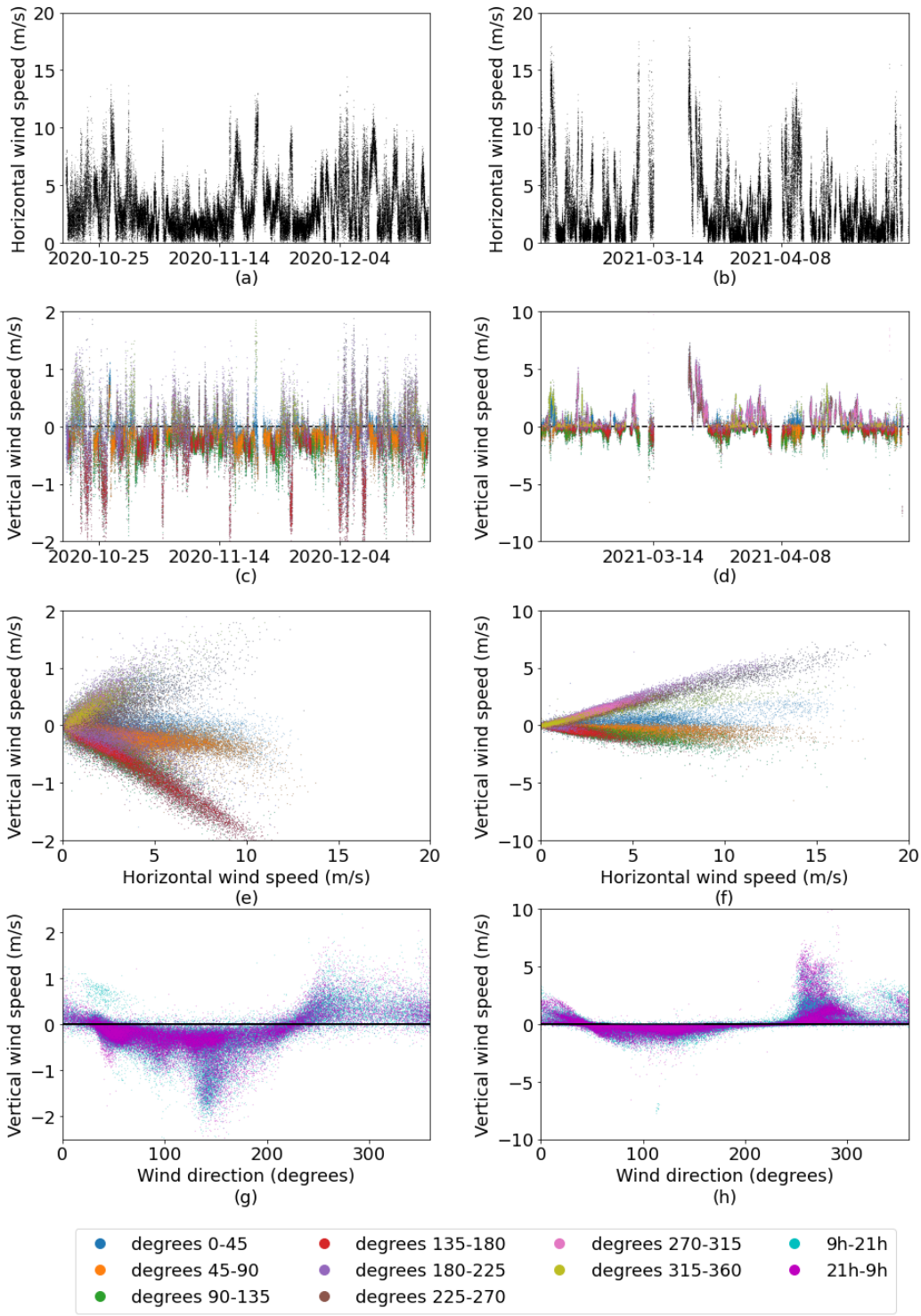

Figure 4 (a) and (b) Horizontal and (c) and (d) vertical wind speed from 3D ultra-sonic anemometer measurements at the Lukmanier and Les Diablerets site, respectively. Correlation between horizontal and vertical wind speed for Lukmanier (e) and Les Diablerets site (f). In (c), (d), (e) and (f) the wind direction is color coded. Correlation between vertical wind speed and wind direction for Lukmanier (g) and Les Diablerets site (h), with a color coding for daytime and nighttime data points.

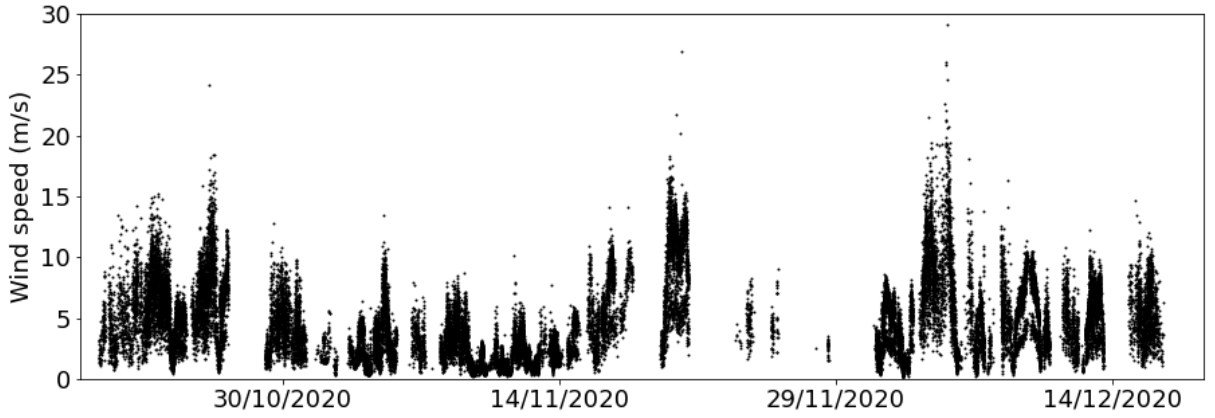

(a)

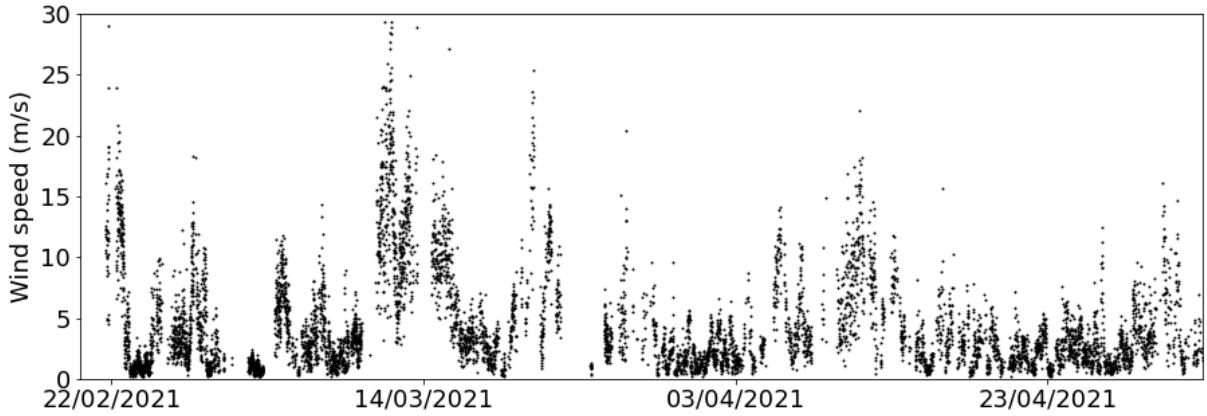

(b)

Figure 5 Horizontal wind speed at 100 m a.g.l. from LIDAR measurement at (a) Lukmanier between 20/10/2020 and 16/12/2020 and (b) Les Diablerets between 20/02/2021 and 02/05/2021.

We choose the height of 100m above ground for the analysis. Figure 7a,b shows the horizontal wind speed from the LIDAR at 100m a.g.l. at the Stadera and Cabane sites. Figure 5c,d show the wind rose at 100m a.g.l. using the LIDAR measurements at the Stadera and Cabane sites, respectively. We see that the principal wind direction at Stadera is more concentrated around the NNE and the Southerly sectors, compared to the near-surface wind rose. The NNE (and S) wind is more likely the synoptic wind from the northerly (or southerly) direction not affected by katabatic effects but more influenced by the valley-scale terrain effect, compared to the results in Section 4.1. Further air flow mechanisms from the surrounding area are explained by the WRF-COSMO1 model simulation results (Section 4.4).

For the Stadera site, the wind speed statistics from the LIDAR measurements at 100m a.g.l. show an average wind speed of 5 m/s, which is higher than the near-surface wind speed average of 3 m/s. The maximum wind speed during the observation period of two months is 31.1 m/s for a wind direction of 158° on 5/12/2020 at 00:17. The timing of this maximum wind event agrees well with the maximum wind measurement from the sonic anemometer.

A shift with height of the principal wind direction sectors is also observed at the Cabane site, where we observe a shift of the Westerlies to the WSW sector compared to the corresponding near-surface wind rose. We further

see an increased wind speed coming from the ENE sector, compared to the wider spread wind directions between NE and SE directions as recorded by the sonic anemometer. This may be a result of the absence of katabatic effects aloft the western face of the Les Diablerets mountain compared to the flow near the ground. The shift of wind direction between ground and 100m level reveals the important effect of the topography as well as thermal processes such as formation of katabatic flow, while aloft at 100m a.g.l., the main topography features, such as the orientation of a mountain ridge or a deep valley plays a controlling role.

The wind speed statistics from the Cabane LIDAR measurements at 100m a.g.l. show an average wind speed of 4.6 m/s, and maximum of 29.4 m/s from a direction of 270° on 11/3/2021 at 21:24. The wind speed maxima occur at a slightly different time period compared to the maximum observed by the sonic anemometer near the ground but during wind from the same westerly sector.

For both study sites (Stadera and Cabane) similar values of average and maximum wind speeds are observed, despite their spatial distance (eastern and western part of Switzerland), different complex topography, and the different observation period. These similar statistics may be explained by the similar altitude above sea level (Table 1). This comparison also shows that katabatic effects are less prevalent further aloft. Finally, results show that with vertical distance from the ground wind direction rather follows the axis of the main terrain features such as mountain ridges or valley axes, rather than small-scale topographical features such as gullies, local plateaus, etc.

4.3. Wind Speed Prediction

A machine learning algorithm is used to combine IMIS weather station data (Section 3) with the LIDAR measurements to predict the wind speed at the campaign site covering long time spans based on the limited-time LIDAR observations used as a training dataset. The long-term hourly wind speed values predicted by the neural network are then used to create the Weibull Distribution. Wind speed is predicted for 20 m and 50 m a.g.l. (Figure 8). Overall, both model approaches of prediction based on u and v on the one hand, and the wind velocity on the other hand, are giving a similar result. For the analysis of the Stadera site, there is a slight decrease of wind speed from the 20m to the 50m a.g.l using the u and v wind component approach. However, we see the opposite trend when using the velocity approach. This may be because the model is having problems with changes in wind directions. We suggest using the velocity approach when we have big changes in wind direction. For validation, former mast measurement results from a campaign by Meteotest in 2016 are used (Figure 9). The Weibull distribution shows an average wind speed of 3.7 m/s at 25 m a.g.l. Our prediction at 20 m a.g.l shows an average wind speed of 4.0 m/s by using the u and v wind component approach for the period of 2010-2020 and 4.1 m/s by using the velocity approach for the period of 2010-2020.

Table 7 Weibull parameters compared with the model prediction at the 20 m a.g.l and 50 m a.g.l

u and v wind component approach				
Height [m.a.g.l]	Duration [year]	Weibull parameters		Average wind speed from model prediction [m/s]
		A	K	
20	2019	4.75	1.50	4.28
	2010-2020	4.30	1.36	3.95
50	2019	4.74	1.52	4.27
	2010-2020	4.30	1.39	3.92
Velocity approach				
Height [m a.g.l]	Duration [year]	Weibull parameters		Average wind speed from model prediction [m/s]
		A	K	
20	2019	4.70	1.84	4.15
	2010-2020	4.61	1.99	4.07
50	2019	5.05	1.98	4.45
	2010-2020	4.91	2.13	4.33

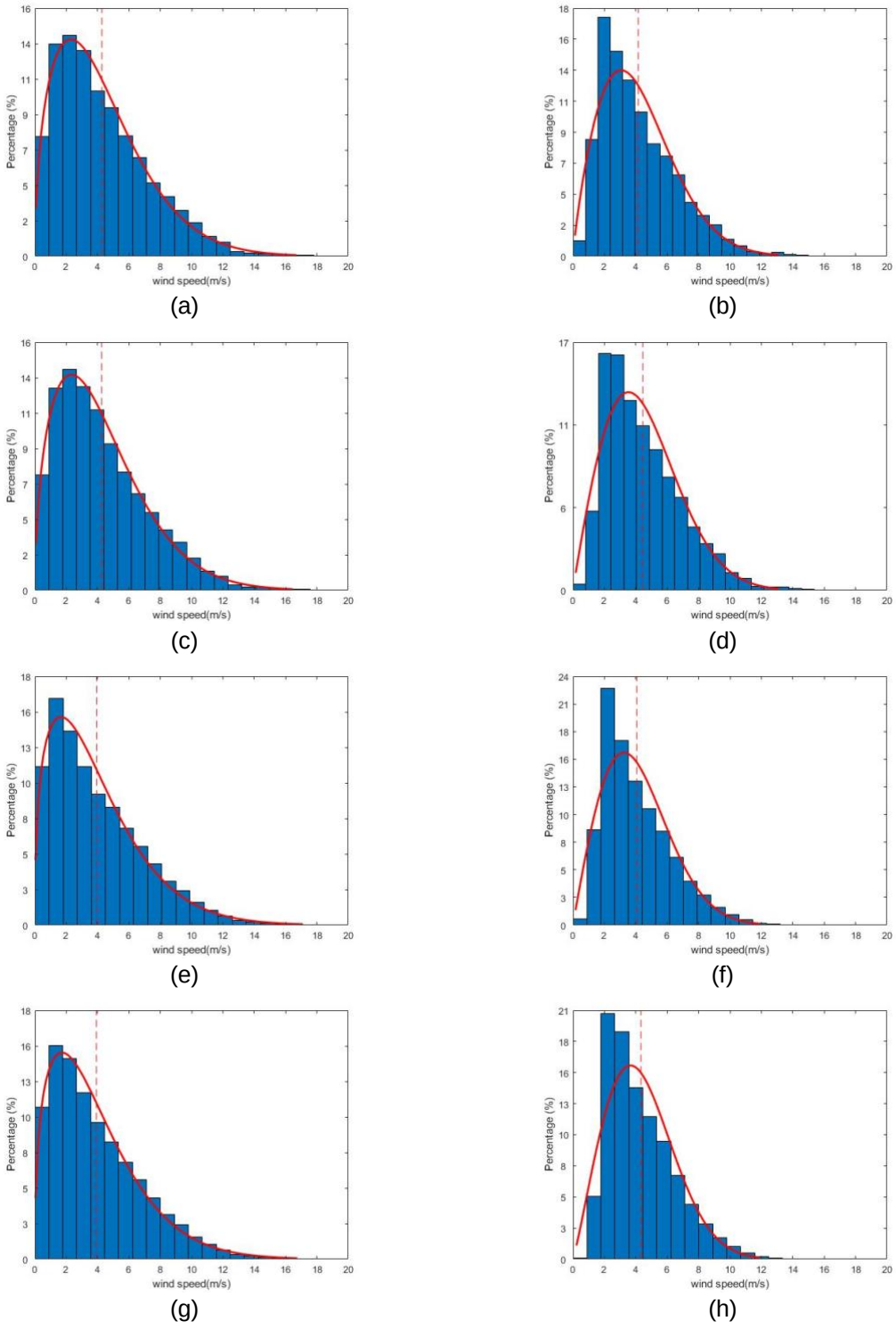

Figure 6 Weibull distribution of the wind speed (m/s) at Lukmanier site for the year of 2019 at 20 m a.g.l. from the uv wind component approach (a) and the velocity approach (b) and at 50 m a.g.l. from the uv wind component approach (c) and the velocity approach (d). Weibull distribution for 10 years period (2010 – 2020) at 20 m a.g.l. from the uv wind component (e) and the velocity approach (f) and at 50 m a.g.l. from the uv wind component approach (g) and the velocity approach (h). The red line shows the Weibull distribution and the red dashed line shows the mean wind speed.

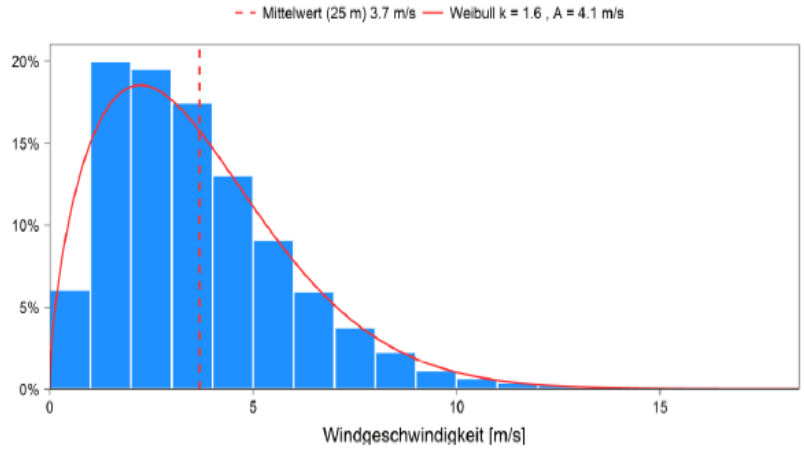

Figure 7 Weibull distribution from the Meteotest campaign at 25 m a.g.l. The red line shows the Weibull distribution and the red dashed line shows the mean wind speed. Source: Meteotest.

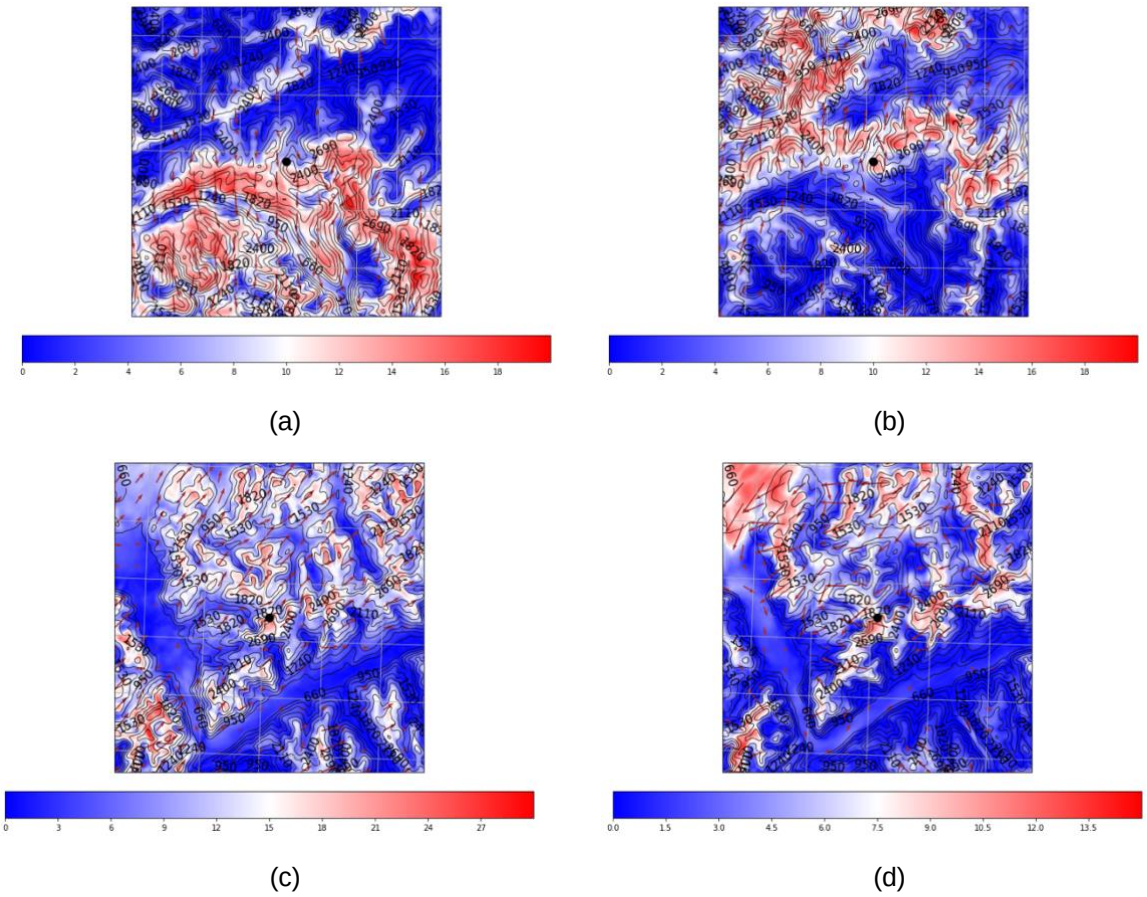

Figure 8 Daily averaged wind speed from WRF-COSMO1 simulation results at 100 m a.g.l. for: the Lukmanier site at (a) 09/12/2020 for northeasterly flow and (b) 23/10/2020 for southwesterly flow; the les Diablerets sit at (c) 27/02/2021 for southwesterly flow and (d) 11/03/2021 for northeasterly flow. The brown arrows show the wind vectors at 100 m a.g.l., the colorbar shows the wind speed and the black dots show the campaign locations.

4.4. Spatial Wind Speed Analysis

We run a WRF-COSMO1 simulation at both sites (see Figure 1 for the model domain) for the two dominating weather regimes. The simulation results are validated by comparison of the wind speed from surrounding IMIS stations, the COSMO 1 km simulation, and the simulation output of the WRF model. Figure 11 shows the comparison between the WRF-COSMO1 (black line), COSMO as input model (green line) and observation results from the IMIS weather stations (blue line).

Figure 11a,b shows the comparison for the southwesterly (27/02/2021) and northeasterly (11/03/2021) flow cases at the Cabane site. The case of northeasterly (09/12/2020, Figure 11d) and southwesterly (23/10/2020, Figure 11c) flows at the Stadera site (SLFLU2, see Table 4) also shows a good agreement between the simulation result and the input from COSMO1. Overall, COSMO1 simulations often show an overestimation of wind speed compared to the observation. As our model uses COSMO1 as its input data, it is also expected that any errors or departures from observations propagate to our model, therefore reproducing a slight overestimation. However, from the comparison we also see that our model performs well in capturing temporal fluctuations of wind speed which are not resolved by the COSMO1 model (Figure 11b). During the period of 11/03/2021 around 21:00, the COSMO1 simulation shows an increase of wind speed and the observation result of the CDM (see Table 5) shows a decrease of wind speed. WRF-COSMO1 was able to correct the errors of COSMO1 and gives a similar result as recorded by the weather stations. This result gives confidence in using the WRF-COSMO1 model to further study the spatial flow patterns in complex terrain in view of optimally exploiting potential for wind power production.

Figure 10 shows the temporally averaged and spatially resolved result of the simulated wind speed at 100 m a.g.l. with the brown arrows indicating the simulated wind vectors. The black dot represents the LIDAR location on the map. For the northeasterly flow case (Figure 10a, 09/12/2020), the wind is coming from the north and is slightly deflected due to the topography (Piz Vallatscha / Scopi). We also notice an acceleration of wind speed when the air flows across the complex terrain of the Swiss Alps. The high wind speed area is mostly located at the southern side of the principal mountain ridges due to the acceleration effect after passing a high obstacle. An opposite mechanism is seen on Figure 10b (23/10/2020), presenting a situation of synoptic wind from the south. As a result, we can use the knowledge about the impact of complex terrain on the principal wind direction and its local modification for finding the most favourable locations for wind energy production in complex alpine terrain.

One of the prominent features in the larger area around the Cabane site is the large, U-shaped Rhone valley. For the south-westerly wind regime at the Cabane site (Figure 10c), most of the high wind speed area is located at high elevation areas. A lower velocity flow can be seen up the Rhone valley. The simulation result from the north-easterly flow case has a higher wind speed compared to the south-westerly flow case (Figure 10d). Low wind speed patterns are seen in the Rhone valley for the two wind patterns. We also see a rather heterogeneous wind direction pattern for the north-easterly flow case compared to the south-westerly flow situation. These simulation results emphasize the importance of understanding the interplay between complex terrain and wind direction to be able to harvest the optimal locations for wind energy over complex alpine terrain in Switzerland.

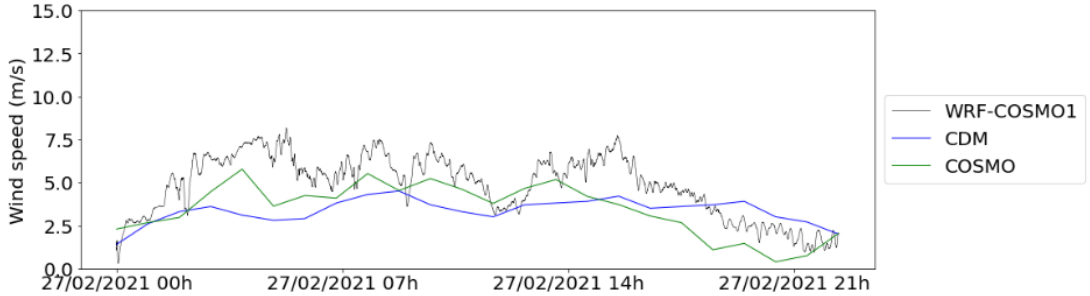

(a)

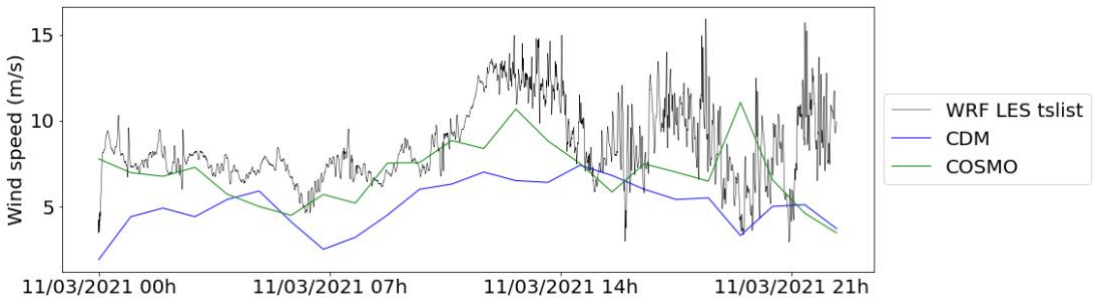

(b)

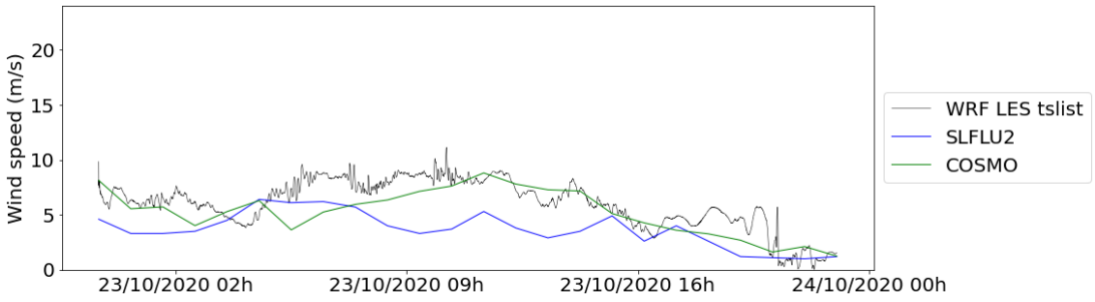

(c)

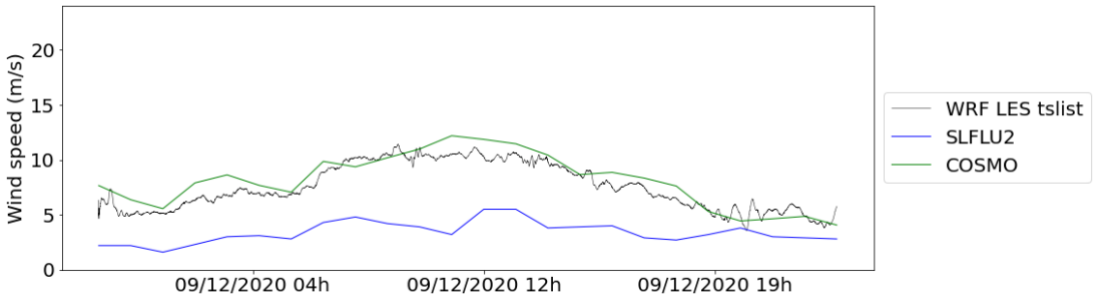

(d)

Figure 9 Wind speed comparison from WRF-COSMO1, COSMO and IMIS stations of Les Diablerets domain CDM sites at (a) 27/02/2021 and (b) 11/03/2021; and Lukmanier domain SLFLU2 sites at (c) 23/10/2020 and (d) 09/12/2020

4.5. Comparison of Various Wind Models and Interpretation of Spatial Wind Potential

In this section, we combine the analysis from various wind models and interpret the results with respect to wind potential estimates previously available. The primary aim is to investigate in how far these results suggest differences to the current estimates from the wind atlas. Three areas with the size of 10 km x 10 km on Les Diablerets, Lukmanier and Buchs are chosen. For Lukmanier and Les Diablerets area, the measurement location is set to be in the center. The measurement location is shown with the star symbol and the wind speed is shown with the colorbar. For the WRF-COSMO1 analysis, the wind direction is shown by the arrows. For analysis, the average of 100 magl annual wind speed from the wind atlas is extracted. For comparison, we also produce 100 magl annual wind speed average from WindTopo. The input data was obtained from 2017 COSMO1 runs with combination of measurement data from automatic weather station. For Lukmanier and Les Diablerets area, we also picked several major wind flow patterns and simulate it using WRF-COSMO1 and Wind-Topo. An additional comparison with the NTB method on St Gallen area at 100 magl is also presented in Figure 14.

On Les Diablerets site (Figure 12a), Wind-Topo (Figure 12e) shows a slightly higher wind speed range compared to the wind atlas (Figure 12b). The spatial distribution of wind speed from Wind-Topo and the wind atlas is showing a similar pattern. Wind-Topo shows somewhat higher wind speeds at exposed locations. For this site, the high wind speed is mostly located at higher elevations. Two wind patterns of southwesterly (Figure 12c,f, 11/03/2021) and northeasterly (Figure 12d,g, 27/02/2021) flows are chosen to be simulated with WRF. From the wind pattern simulations we can see that the high wind speed areas change location. Both WRF-COSMO1 simulations (Figure 12c,d) show a higher wind speed on the leeward side, respectively. This indicates downslope winds under stable atmospheric conditions during the winter days rather than flow separation. Locations of downslope winds are potential areas for wind farm development. Wind-Topo results were also extracted for these two flow situations (Figure 12f,g). The results of spatial wind distribution show a similar shape, with WRF COSMO1 showing a smoother and somewhat wider distribution of high wind speeds. It is remarkable that Wind-Topo appears to capture location and strength of high-wind zones when compared to WRF. The smoother fields can be explained by using a lower grid (and topography) resolution. Overall, the comparison validates the yearly estimates from the wind atlas.

On the Lukmanier site (Figure 13a), the wind atlas (Figure 13b) also shows a pattern of high wind speed at high elevations, mostly following the ridgeline. Wind-Topo (Figure 13e) shows that higher wind speeds should affect larger areas than suggested by the wind atlas. In addition, Wind-Topo shows clearly higher wind speeds over the ridgelines. Interestingly, Wind-Topo also shows clearly higher wind speeds along the axis of the main valley (Lai Da Sontga Maria). This could be the effect of channeling over Passo Lucmagno. For further analysis, two wind patterns of northerly (Figure 13c,f, 09/12/2020) and southerly (Figure 13d,g, 23/10/2020) are simulated with WRF-COSMO1 and Wind-Topo. From the northerly case, we also see the high wind speed area located on the Lai Da Sontga Maria. The high wind speed could be the result of channeling from the northerly wind passing through Passo Lucmagno. When the wind finally reaches Pizzo dell'Uomo, on the south of Lai Da Sontga Maria, a further slight increase in wind speed towards the South is observed from the result of WRF-COSMO1 and Wind-Topo. Similar to Les Diablerets, we see areas of high wind speed on the leeward side from both northerly and southerly simulation of WRF. For this site, we can conclude that Wind-Topo predicts higher wind potential over larger areas than the wind atlas and that these results are supported by WRF simulations for specific flow simulations. Again, similar to Les Diablerets, WRF simulations show smoother fields caused by coarser and smoother terrain input.

On the Buchs area (Figure 14a), in general, the wind atlas (Figure 14c) and Wind-Topo (Figure 14d) shows a similar pattern of high wind speeds for the annual average. However, there is a slightly different pattern on the Regitzer Spitz. The wind atlas shows high wind speeds mostly on the ridgeline, while Wind-Topo shows organized and extended areas of high wind speeds to both sides of the main ridge. Note that the organized high-wind structures are also caused by transversal ridges, not resolved in WRF simulations. For comparison, we also show a comparison with the earlier NTB result (Figure 14b), but due to the different area, resolution and the fact that NTB results are given as power potential, we can only compare patterns. The NTB analysis is roughly comparable to the wind atlas. The finer-scale patterns such as on Registzer Spitz are not resolved on the NTB maps.

Overall, from the three sample areas that we analyzed, the wind atlas appears to capture high-wind areas in particular over the ridges. Wind-Topo and WRF-COSMO1, on the other hand, are shown to be in partial agreement with the wind atlas but also show that some areas of higher wind speeds may be missed by the wind atlas. This comparison has shown the importance to add the element of topographic effect to the spatial distribution of wind potential mapping in Switzerland.

4 National and international cooperation

Acknowledgements to Silvio Candinas, Clemens Berther and their team (armasuisse), Bernhard Tschannen and Urs von Siebenthal and their team (Glacier3000), Halo Photonics onsite support, CSCS.

5 Publications

-

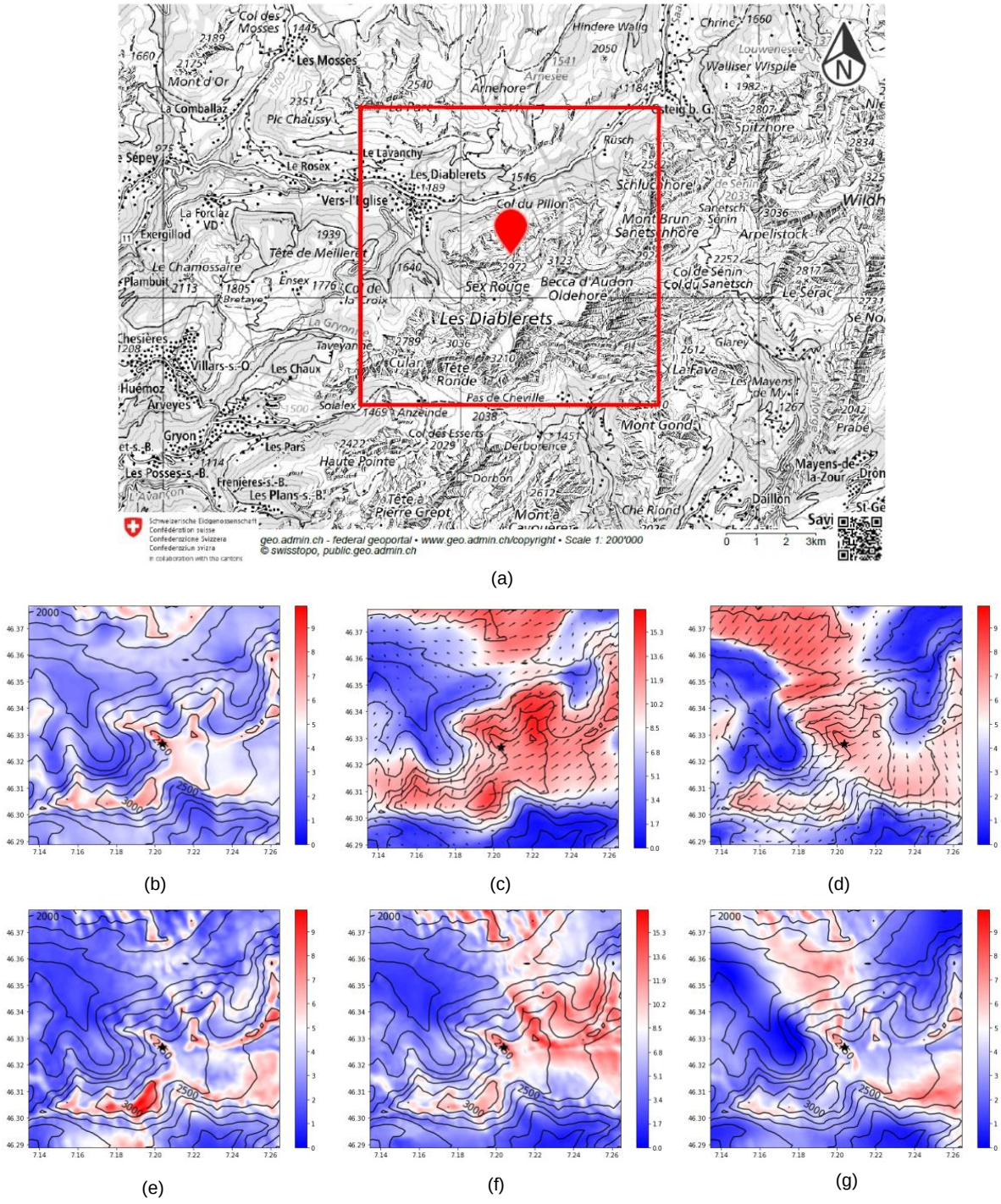

Figure 12 Comparison analysis for the mean wind speed on the Les Diablerets area shown in map of (a) at 100 magl from (b) the wind atlas and (e) Wind-Topo. Sample from (c,f) southwesterly 11/03/2021 00h00-04h00 and (d,g) northeasterly 27/02/2021 00h00-02h00 wind pattern taken from (c,d) WRF simulation and (f,g) Wind-Topo at 100magl. Colorbar shows the mean wind speed in m/s. Star symbol shows the location of the campaign.

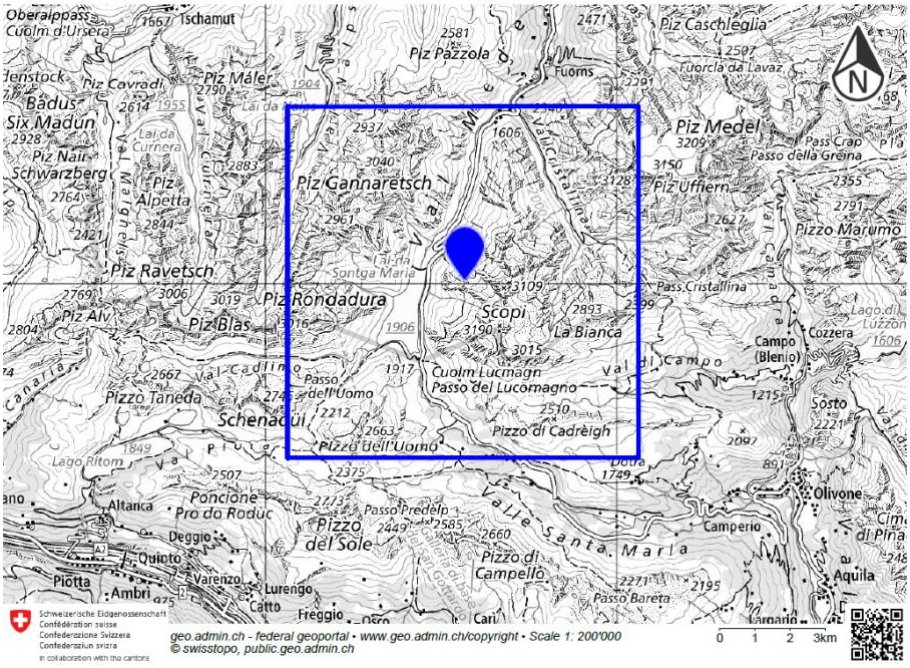

(a)

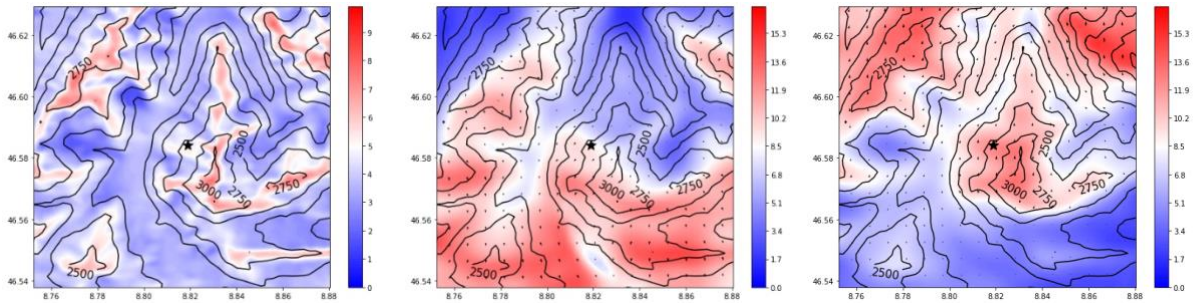

(b) (c) (d)

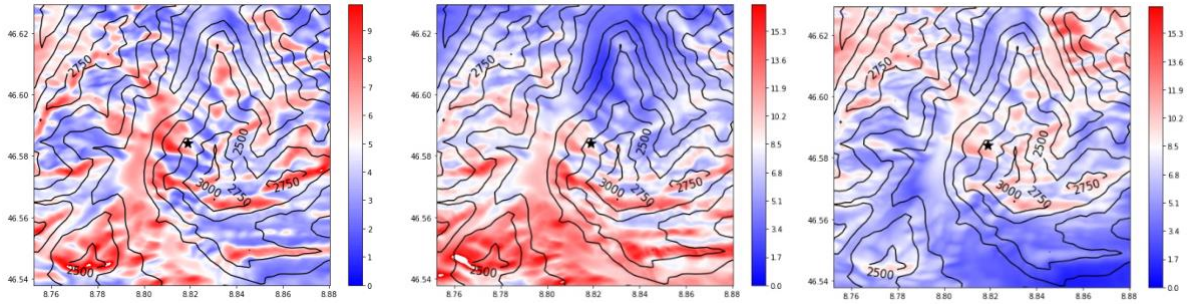

(e) (f) (g)

Figure 13 Comparison analysis for the mean wind speed on the Lukmanier area shown in map of (a) at 100 magl from (b) the wind atlas and (e) Wind-Topo. Wind pattern simulation of (c,f) northerly 09/12/2020 and (d,g) southerly 23/10/2020 taken from (c,d) WRF simulation at 70 magl and (f,g) Wind-Topo at 100 magl. Colorbar shows the mean wind speed in m/s. Star symbol shows the location of the campaign.

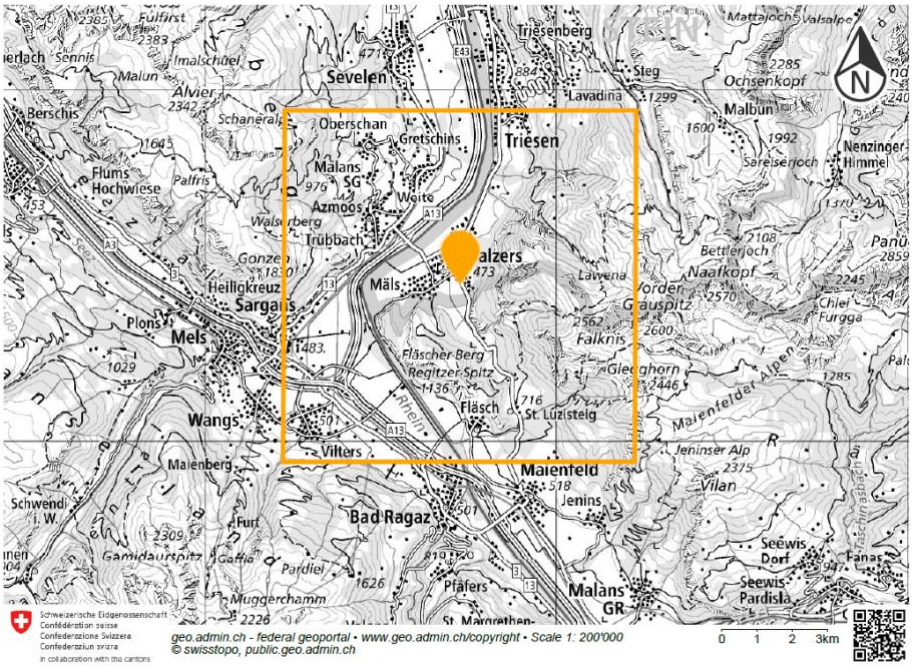

(a)

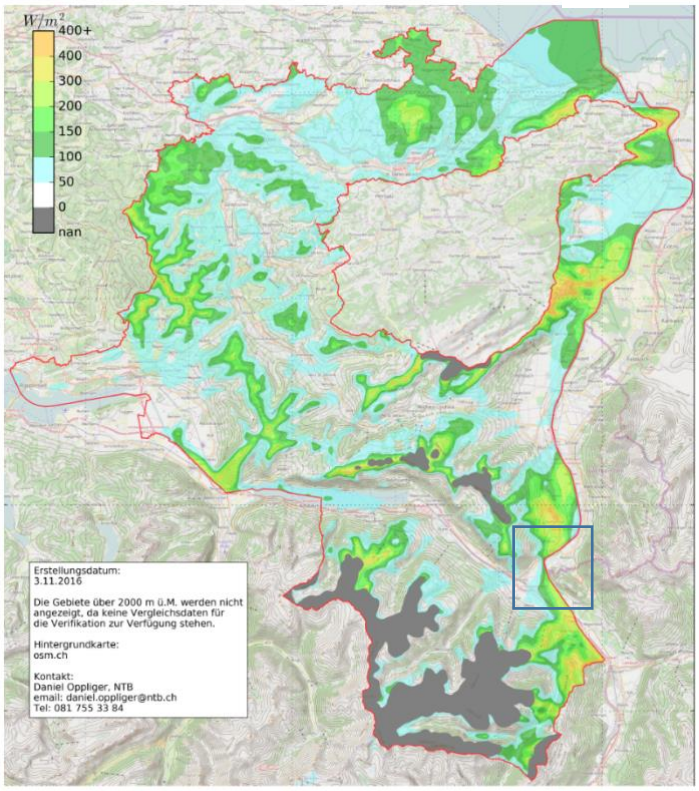

Abbildung 32: Windleistung 100m über Grund

(b)

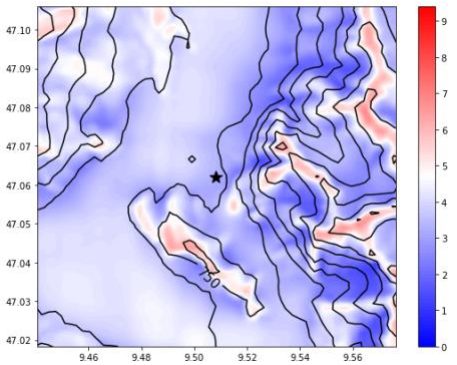

(c)

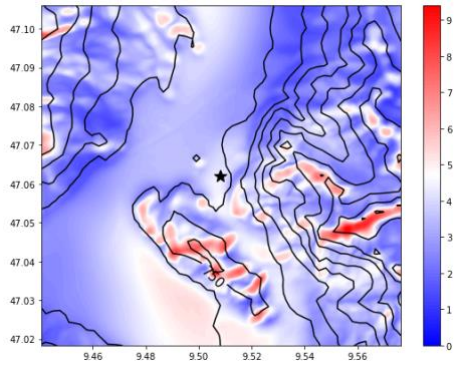

(d)

Figure 14 Comparison analysis for the mean wind speed on the Buchs area shown in map of (a) at 100 magl from (b) NTB method, (c) Wind Atlas Switzerland and (d) WindTopo. Colorbar shows the mean wind speed in m/s. Star symbol shows the location of the campaign. Blue box in Figure (b) shows the domain range of Wind-Topo.

6 References

[1] Archer, C. L., & Jacobson, M. Z. (2005). Evaluation of global wind power. *Journal of Geophysical Research: Atmospheres*, *110*(D12)

[2] Brower, M. (2012). *Wind resource assessment: a practical guide to developing a wind project*. John Wiley & Sons.

[3] Chow, F. K., Schär, C., Ban, N., Lundquist, K. A., Schlemmer, L., & Shi, X. (2019). Crossing multiple gray zones in the transition from mesoscale to microscale simulation over complex terrain. *Atmosphere*, *10*(5), 274.

[4] Clifton, A., Daniels, M. H., & Lehning, M. (2014). Effect of winds in a mountain pass on turbine performance. Wind Energy, 17(10), 1543-1562. https://doi.org/10.1002/we.1650

[5] European Environmental Agency (2006). CORINE Land Cover (CLC) 2006 raster data,Version 13, https://www.eea.europa.eu/dataand-maps/data/clc-2006-raster, downloaded: 2016-06-15, accessed: 2021-06-28

[6] Dujardin, J. and Lehning, M. (2022), "Wind-Topo: Downscaling near-Surface Wind Fields to High-Resolution Topography in Highly Complex Terrain with Deep Learning." QJRMS, https://doi.org/10.1002/qj.4265.

[7] Franziska Gerber; Michael Lehning (2021). High resolution static data for WRF over Switzerland. EnviDat. doi: 10.16904/envidat.233.

[8] Grams, C. M., Beerli, R., Pfenninger, S., Staffell, I., & Wernli, H. (2017). Balancing Europe's wind-power output through spatial deployment informed by weather regimes. *Nature climate change*, *7*(8), 557-562

[9] Iacono, M. J., Delamere, J. S., Mlawer, E. J., Shephard, M. W., Clough, S. A., & Collins, W. D. (2008). Radiative forcing by long-lived greenhouse gases: Calculations with the AER radiative transfer models. *Journal of Geophysical Research: Atmospheres*, *113*(D13).

[10] Jiménez, P. A., Dudhia, J., González-Rouco, J. F., Navarro, J., Montávez, J. P., & García-Bustamante, E. (2012). A revised scheme for the WRF surface layer formulation. *Monthly weather review*, *140*(3), 898-918.

[11] Sara Koller and Tanja Humar. Windpotentialanalyse fürWindatlas.ch: Jahresmittelwerte der modellierten-Windgeschwindigkeit undWindrichtung. Schlussbericht. Technical report, MeteoTest, BFE, 2016

[12] Meteotest, Windenergieprojekt Staderas, 2016.

[13] Mirocha, J. D., Lundquist, J. K., & Kosović, B. (2010). Implementation of a nonlinear subfilter turbulence stress model for large-eddy simulation in the Advanced Research WRF model. *Monthly Weather Review*, *138*(11), 4212-4228

[14] Moeng, C. H., Dudhia, J., Klemp, J., & Sullivan, P. (2007). Examining two-way grid nesting for large eddy simulation of the PBL using the WRF model. *Monthly weather review*, *135*(6), 2295-2311.

[15] Morrison, H., Thompson, G., & Tatarskii, V. (2009). Impact of cloud microphysics on the development of trailing stratiform precipitation in a simulated squall line: Comparison of one-and two-moment schemes. *Monthly weather review*, *137*(3), 991-1007.

[16] NASA/METI/AIST/Japan Spacesystems and U.S./Japan ASTER Science Team (2019). ASTER Global Digital Elevation Model V003, NASA EOSDIS Land Processes DAAC, distributed by NASA EOSDIS Land Processes DAAC, accessed 2021-06-28, at https://doi.org/10.5067/ASTER/ASTGTM.003

[17] Niu, G. Y., Yang, Z. L., Mitchell, K. E., Chen, F., Ek, M. B., Barlage, M., ... & Xia, Y. (2011). The community Noah land surface model with multiparameterization options (Noah-MP): 1. Model description and evaluation with local-scale measurements. *Journal of Geophysical Research: Atmospheres*, *116*(D12).

[18] SFOE (2018) Energy Strategy 2050. https://www.bfe.admin.ch/bfe/en/home/policy/energy-418 strategy-2050.html. Last access: 9 December 2021

[19] SFOE (2022). Wind Atlas of Switzerland. https://www.uvek-gis.admin.ch/BFE/storymaps/EE_Windatlas/?lang=en Last access: 21 February 2022

[20] Shin, H. H., & Hong, S. Y. (2015). Representation of the subgrid-scale turbulent transport in convective boundary layers at gray-zone resolutions. *Monthly Weather Review*, *143*(1), 250-271.

[21] Skamarock, W. C., Klemp, J. B., Dudhia, J., Gill, D. O., Liu, Z., Berner, J., ... & Huang, X. Y. (2019). A description of the advanced research WRF model version 4. *National Center for Atmospheric Research: Boulder, CO, USA*, *145*, 145.

[22] Yang, Z. L., Niu, G. Y., Mitchell, K. E., Chen, F., Ek, M. B., Barlage, M., ... & Xia, Y. (2011). The community Noah land surface model with multiparameterization options (Noah-MP): 2. Evaluation over global river basins. *Journal of Geophysical Research: Atmospheres*, *116*(D12).